Robot-Assisted Decompressive Laminectomy Planning Based on 3D Medical Image

YU SUN[1,2], ZHONGLIANG JIANG[3], XIAOZHI QI[3], YING HU[3], (Member, IEEE),
BING LI[1], (Senior Member, IEEE), AND JIANWEI ZHANG[4], (Member, IEEE)

[1]Harbin Institute of Technology, Shenzhen 518052, China
[2]CAS Key Laboratory of Human-Machine Intelligence-Synergy Systems, Shenzhen Institutes of Advanced Technology, Chinese
Academy of Sciences, Shenzhen 518055, China
[3]Shenzhen Key Laboratory of Minimally Invasive Surgical Robotics and System, Shenzhen Institutes of Advanced Technology, Chinese Academy of Sciences,
Shenzhen 518055, China
[4]Department of Informatics, University of Hamburg, 22527 Hamburg, Germany

Corresponding authors: Ying Hu (ying.hu@siat.ac.cn) and Bing Li (libing.sgs@hit.edu.cn)

ABSTRACT The decompressive laminectomy is a common treatment for lumbar spinal stenosis. Generally, surgeons use grinding tools to remove laminae under the guidance of intraoperative medical images. To improve accuracy and reduce surgeons' burdens, robot-assisted surgery is gaining acceptance. This paper proposes a method to plan grinding paths and velocities based on 3-D medical images in the context of robot-assisted decompressive laminectomies. As the lesion areas to be grinded are irregular, an interactive method with 3-D reconstruction is designed for surgeons to transfer discrete information about grinding paths and velocities to the robot system. The path generation strategy is based on a ray casting algorithm after space registrations, while the velocity generation strategy is based on the virtual force and mechanical analysis is used to optimize temporal efficiency and stability. A complete system is developed to test and explore the feasibility of this method. Results suggest that robot-assisted decompressive laminectomies can be performed well.

INDEX TERMS Surgical robot, decompressive laminectomy, 3D image interaction, path planning, image-driven velocity.

I. INTRODUCTION

Lumbar spinal stenosis (LSS) is a common orthopedic complaint that causes a series of neurological symptoms [1], [2]. The decompressive laminectomy is a way of treating LSS, in which the lamina is wholly or partially removed, via unilateral or bilateral fenestration, using a high-speed burr or piezosurgery to reduce the risk of spinal cord injuries [3]–[6]. In long-time freehand operations, the grinding allowance can be difficult to control and exacerbated by surgeons' physical fatigue, which may cause serious damage to patients [7]. As shown in Fig. 1, hyperplasia or ossification of the ligamentum flavum causes LSS, and the unilateral lamina is grinded to a certain thickness to help relieve compression.

Compared with freehand operations, surgical robots offer advantages in terms of higher accuracy and reliability, ease of interaction, substantially less scope for human fatigue, and reduced risk of complications [8]–[10]. The first robot system developed for assisting orthopedic operations was the Robodoc system (Curexo Technology Corp, America). Using this technology, surgeons can customize the grinding scheme based on computed tomography (CT) images before operations [11]. Later came the RIO system (MAKO Surgical Corp, America), which can restrict operations by reverse driving force and real-time navigation [12]. For spinal surgery, MazorX and Renaissance systems (Mazor Robotics Corp, America) are series and parallel structures, respectively; they are used to place pedicle screws based on CT images and navigation [13]. These systems have different operation-specific planning functions. For knee replacements, the femoral head is completely labelled after 3D reconstruction, and such operations proceed using a constant grinding velocity. For spinal
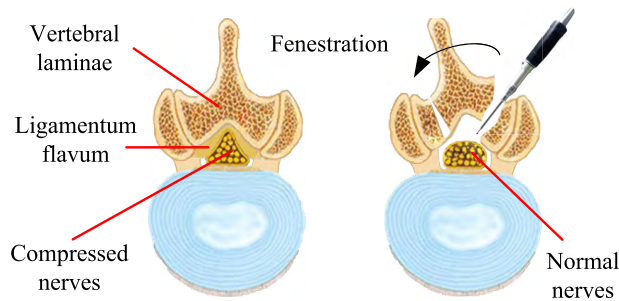
FIGURE 1. Compressed nerves caused by hyperplasia of ligamentum flavum (left image) and normal nerves after unilateral fenestration (right image).

implants, only two coordinates in a 3D image are needed to determine the target screw path. However, the lesion areas in decompressive laminectomies are irregular, and grinding tends to be used locally with strict boundary requirements. This paper proposes a methodology to plan the grinding path and velocity based on 3D medical images for decompressive laminectomies. The planning system includes 3D reconstruction, interaction, registrations, path generation, and image-driven velocity.

The CT volume is grid structure data, where each cell is assigned a volume fraction [14]. Lorensen and Cline [15] developed a marching cubes algorithm to create triangle models of constant density surfaces from volume data. Lewiner *et al.* [16] configured more accurate topological models through look-up table improvements. Lopes and Brodlie [17] modified the marching cubes algorithm for isosurfacing to improve its robustness under perturbations of the data and threshold value. Vignoles *et al.* [18] proposed a simplified marching cubes algorithm without the need for interpolation. The marching cubes algorithm is important for the 3D reconstruction of CT data, which is the basis of surgical planning. Segmentation is often performed on medical images for diagnosis and treatment planning. As medical images are noisy and lack contrast, segmentation represents a major bottleneck in practical application [19]. Segmentation can be used to extract tissue and perform independent reconstruction. Marian [20] automated the conventional region-growing technique without initialization. Stawiaski *et al.* [21] proposed an interactive segmentation method based on graph cuts. Li *et al.* [22] proposed a novel region-based level-set method for image segmentation. Dakua and Abi-Nahed [23] developed a method for image segmentation based on stochastic resonance theory. Although these methods can improve the accuracy of reconstructions, doing so is not necessary in practical applications. As the lamina is objectively distinct from surrounding soft tissues and lacks sharp edges and corners, reconstruction in this area is usually smooth. Therefore, a bounding box is designed for surgeons to extract the lamina structure freely and conveniently.

In robot-assisted surgery, robot-to-patient and patient-to-image registrations provide real-time position information

in the image system, which helps the surgeon to maintain the requisite position and orientation. Intensity-based 3D to 2D rigid registration is the most common method used in orthopedic surgery. Penney *et al.* [24] and Khamene *et al.* [25] determined that the pattern intensity and gradient difference performed best in registration. Maes *et al.* [26] explored how various search strategies with respect to rigid and non-rigid registration differentially affected precision and convergence. Demirci *et al.* [27] introduced interpolation and stent-editing techniques to handle occlusion and dissimilarity during registration. Schwerter *et al.* [28] used this technique to recover and visualize the position of tools during interventional surgery. Landmark-based registration exhibits higher accuracy and clinical practicality because patient-specific volume data can be collected during the operation. Hajeer *et al.* [29] developed a software-based facial analysis tool to evaluate the reproducibility of landmark identification. Verhoeven *et al.* [30] assessed the efficacy of four registrations for quantifying facial asymmetry. The most common algorithm used for registration is the iterative closest point (ICP) algorithm. For further application, we construct a registration block to realize space registrations automatically; this avoids the errors and temporal inefficiencies associated with manual operations by surgeons.

Velocity control during lamina grinding is important to ensure the quality of operations and minimize robot inefficacies caused by uncertainties inherent in complex environments. Accordingly, intraoperative state recognition and control techniques have received wide attention. State expressions mainly include force and torque, current, sound and vibration, etc. [31]–[41]. The force signal is widely used as the input to the feedback control system of the robot because its components are simple. With force coupling, the current signal can also reflect the state of robot operations after filtration. Wang *et al.* [42] proposed a robot grinding system for decompressive laminectomies based on force control and revealed that the margin could be stably controlled within 1 mm. Deng *et al.* [43] and Fan *et al.* [44] improved the adaptivity of the robot to the complex surface of laminae based on force fuzzy control. Zaheer *et al.* [45] proposed a modular implementation scheme for fuzzy systems with input uncertainties. Jin *et al.* [46] and [47] derived an explicit bound relationship between input noise and end-effector position error. However, fuzzy control requires real-time feedback from intraoperative signals, which may be noisy and lagged. Moreover, the fuzzy rules need to be artificially designed, and communication needs to be accurate during high-speed transmission. Gray values in medical images contain prior information about bone composition and thus exhibit a coupling relationship with the force signal. Therefore, we define a virtual force to plan the grinding velocity based on mechanical analysis.

The remainder of the paper is organized as follows. Section II describes an interactive 3D image-based methodology for use by surgeons which includes 3D reconstruction and lamina extraction. Section III introduces a method to generate

the grinding path, which includes registrations among the different spaces. Section IV analyzes the on-operation dynamics of a ball-end grinding tool and proposes an image-driven velocity planning method based on virtual force. Section V conducts experiments to explore the feasibility of the proposed method. Finally, conclusions are drawn in Section VI.

II. MEDICAL IMAGE INTERACTION

Image-guided surgical navigation is the key technology to realize precise surgical procedures. Surgeons analyze and plan the patient's lesion area in images, and the output from this exercise is used to guide the robot to complete drilling and grinding. The preoperative CT image has a high resolution and a large imaging range, and the model's surface is smooth after 3D reconstruction which helps surgeons to create accurate plans. However, a 2-3 mm bias is always present because of elastic deformation of the spine. Moreover, the placement of the patient affects the overall shape of the spine. Therefore, an annular scan of the C-Arm can better reflect the actual morphological features of the patient during the operation. The lower definition of X-ray images leads to more noise in 3D reconstruction, which may impede surgeons' planning of operations.

Compared with 2D medical images, 3D images are easy to understand and intuitive for planning. The surgeon can use a mouse to interact with the 3D image and observe the spinal model from different directions. For the decompressive laminectomy, the region of interest (ROI) is the lamina where lesions occur, such as bone hyperplasia, and cause the spinal nerves to be subjected to pressure. Therefore, a convenient interaction method is needed for surgeons to quickly extract the ROI in 3D images. Calculating the coordinates of feature points on laminae is the most important task for robot control.

A. RECONSTRUCTION AND EXTRACTION

The original X-ray image series annularly scanned by C-Arm is often associated with image artifacts focusing on high density objects. Due to differences in radiation attenuation in bone tissue and the discontinuous directions of irradiation, X-ray images have non-uniform intensities that result in overlap in the searching area for some segmentation algorithms, such as region growing. Moreover, the bone boundary is not sufficiently clear after adjusting the window level and width, such that it is difficult to solve the gradient flow equation using the level-set algorithm. Indeed, many segmentation algorithms cannot process X-ray images effectively.

In Fig. 2, the spinal bone is placed in an arbitrary direction and the lamina surface has a certain curvature in 3D space. It is inconvenient to select the area to be removed by clicking the mouse on 2D images layer by layer. Therefore, a 3D bone model is built for interaction based on marching cubes, and a bounding box is created around the reconstructed model for manual selection of the ROI. The salient parameters for X-ray image reconstruction are listed in TABLE 1, and results are shown in Fig. 3.
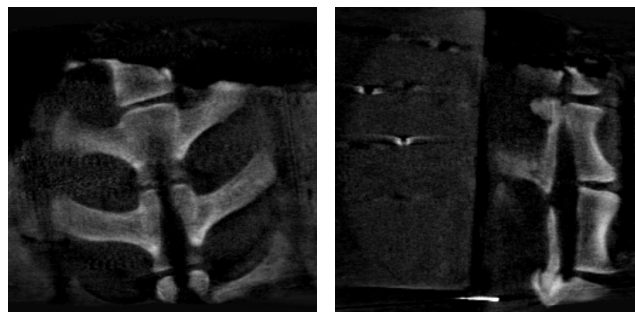

FIGURE 2. X-ray image series of a sheep's spine. The window level and window width are set to 950 and 420, respectively. The displayed images are resampled into an [0, 255] interval.

TABLE 1. Parameters for X-ray image reconstruction.

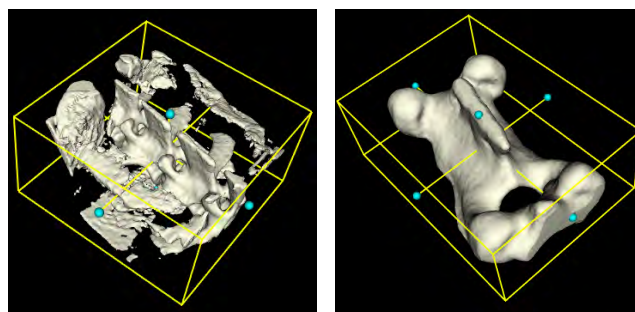| Isoline	Window Level	Window Width
170	690	900

FIGURE 3. Interactive lamina extraction based on a bounding box showing the original 3D image (left) and the extracted lamina where out-of-box pixels are set to the minimal value in the bounding box (right).

In Fig. 3, the original 3D image (left) is noisy, which hinders surgeons from planning optimal paths on the 3D lamina model. The ideal situation is to show only those parts of the lamina that need to be decompressed with model coordinates that are consistent with the original. For medical imaging, the window level range is $[-1000, 1000]$, which means the minimal value -1000 must be converted to zero after reconstruction, and these pixels will appear black. Therefore, creating a new copy where the out-of-box pixels are set to a specified value that is smaller than the in-box pixels can quickly rebuild the required area (right). These functions are implemented and tested on the 3D image system developed by our team.

The initial bounding box has only a translational relation with the image coordinates. The six boundaries **B** also represent the coordinates of the six surfaces of the cube, so it is easy to determine whether a space point is inside the cube. Moreover, the surgeon can adjust the position and size of the box freely according to his or her own needs.

The dynamic bounding box can be obtained from **B** through $\mathbf{T}_b$ transformation. The elements in the $\mathbf{T}_b$ matrix are

---

Algorithm 1 Interactive Extraction

```
1:   B ← initial boundaries [xs xe ys ye zs ze]
2:   foreach pixel
3:       P ← current position [x y z]
4:       IP ← inverse T_b ∗ P
5:       if B[0] > IP[0] or B[1] < IP[0] or
             B[2] > IP[1] or B[3] < IP[1] or
             B[4] > IP[2] or B[5] < IP[2] or
6:       then pixel = specified value (e.g. −1000)
7:   end
8:   three-dimensional median filtering
9:   reconstruct data in marching cubes method
```

---

computed during the interaction between the surgeon and the 3D image in real time. $\mathbf{T}_b$ is not a rigid transformation matrix because of its translation, rotation, and unequal scaling. For any pixel $\mathbf{P}$ in the 3D image, it is convenient to determine whether $\mathbf{P}$ is in the dynamic bounding box after the $\mathbf{T}_b^{-1}$ transformation. Based on this method, volume data can be processed by Algorithm 1.

B. DISCRETE EXPRESSION OF LAMINA

The morphological equation of the lamina is continuous and differentiable. The shape of the lamina surface is patient-specific. Therefore, it is difficult to build a generic mathematic model to describe the grinding path in decompressive laminectomies. The scheme is to realize path planning through surgeon-bounding box interaction. After the lamina model is extracted, the surgeon can adjust the box to enclose the grinded area within the bounding box. The upper and lower surfaces of the bounding box are down sampled to reduce the amount of computation, and the remaining data are sufficient to reflect the morphological features of lamina. Each sampling point is treated as a unidirectional light source that projects along the normal direction to the lamina surface.

As shown in Fig. 4, balls attached to the bone surface are the points of intersection between light and lamina. The upper points set (left) $\mathbf{Q}_m$ describes the morphological features of the upper surface, and the lower points set (right) $\mathbf{Q}_n$ describes the lower surface. Moreover, points set $\mathbf{Q}_n$ is configured as the constraint boundary of robot movements to prevent instruments compromising the inner cortical bone and thus to avoid causing spinal nerve injuries. The distribution of light sources is homogeneous and calculated as follows:

$$s = \frac{b_l}{b_w} \tag{1}$$

where b_l and b_w are the length and width of the upper and lower surface of the bounding box, respectively.

$$s[n_w]^2 + (s+1)[n_w] + (1 - N) \leq 0 \tag{2}$$

where n_w is the number of grids along the width direction, and N is the maximum number of intersection points specified by the surgeon. Herein, N is set to 48.
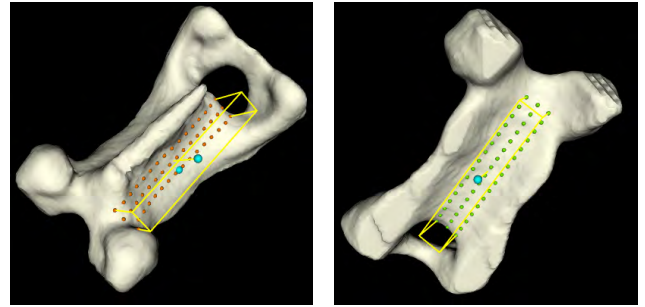

FIGURE 4. Discrete expression of lamina upper surface (left) and lamina lower surface (right).

The number of lights along the width direction is $[n_w] + 1$, where n_w is the maximum value that satisfies formula (2). After rectangular meshing, the intersection points can be searched along the light direction according to given steps. However, to reduce computational complexity, the 3D reconstruction reserves only the data reflecting external surface features; thus, the thickness of the actual volume data is only one pixel and may cross the surface during the search for intersection points because the interior is hollow. For this problem, we use the BSP-Tree method to search intersection points.

III. GRINDING PATH PLANNING

The actual grinding path of the robot is not only $\mathbf{Q}_m$ and $\mathbf{Q}_n$ generated from the 3D image. The data in the image space $\{\mathbf{I}\}$ should be converted into the robot space $\{\mathbf{R}\}$. This process is denoted $\{\mathbf{I}\}$ to $\{\mathbf{R}\}$ registration. It is inconvenient for surgeons to establish the mapping between $\{\mathbf{I}\}$ and $\{\mathbf{R}\}$ directly; we can use a binocular stereo vision system, such as the NDI Polaris Vicra System (Canada), to establish an additional coordinate $\{\mathbf{N}\}$ and collect the target coordinates by reading the positions of the probe tip to complete the registration indirectly. For decompressive laminectomies, the bone can be treated as a rigid body, and the transformation matrix is also a rigid matrix. Therefore, registration is quick when using the ICP method. After the coordinates in space $\{\mathbf{I}\}$ are converted into space $\{\mathbf{R}\}$, the data can be used in robot control.

As the depth of grinding is about 2-6 mm, it is not reasonable to grind down to the specified position in a single intervention. Therefore, an interpolation algorithm is needed to generate more layers for grinding operations. The points in space $\{\mathbf{R}\}$ after registration are distributed in a potential two-dimensional manifold with a small curvature. The Euclidean distances of point pairs existing in upper and lower manifolds, respectively, are different. After interpolation, each layer has a different manifold structure. The grinding path is generated layer by layer, while allowance can be specified if needed. When the robot proceeds along the path, instantaneous acceleration during the grinding operation can be controlled by setting the blend radius, which means arcs instead of sharp angles are used to reduce the impact of movement on the system. This mode can render the robot safer and more stable in grinding operations.
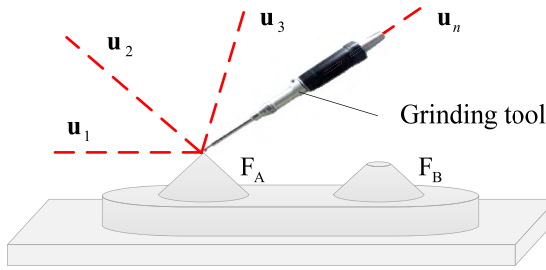
FIGURE 5. Grinding tool offsets calculation based on the least squares method. F_A is a calibration table with a sharp point, whereas F_B is a spherical concave surface. Vector $\mathbf{u}_n$ is the nth pose where n is at least 4 (set to 6 herein).

FIGURE 6. Registration block constructed using PSU material. The material can be transmitted by X-ray. The block is enclosed by six steel balls 1 mm in diameter, distributed asymmetrically in three layers.

A. ROBOT REGISTRATION

The robot registration includes two parts: adding offsets to the end of the robot tool, and establishing the mapping between the two spaces $\{\mathbf{I}\}$ and $\{\mathbf{R}\}$. In our research, medical grinding equipment, the XIYI electrokinetic skeletal system (China), is used. Its maximum speed is constant at 80000 rpm, and it has a spherical emery bit. The position information read from the robot system is the center of its own end $\{\mathbf{E}\}$ in the robot basic coordinate $\{\mathbf{B}\}$; however, the control path works on the edges of the grinding bit $\{\mathbf{G}\}$. The translation offset $_G^E\mathbf{P}$ should be added to the kinematics of the robotic system, while rotation one $_G^E\mathbf{R}$ is treated as per the unit matrix. To generate the robot's spatial path $\{\mathbf{R}\}$, the transform matrix $_I^R\mathbf{T}$ needs to be optimized to establish the mapping of data in space $\{\mathbf{I}\}$.

As shown in Fig. 5, a calibration model is constructed using a 3D printer and then fixed on the experimental platform. There are two kinds of calibration tables, F_A and F_B, for calculating the offsets. F_A has a sharp point for calibration of the specified position on the tool's surface, while F_B has a spherical concave surface for calibration of the center of the spherical tool. In the calibration process, we drag the robot in free drive mode and adjust the position of the grinding bit edge onto the tip of F_A in different poses recorded as vectors set $\{\mathbf{U} \mid \mathbf{u}_1 \, \mathbf{u}_2 \, \ldots \, \mathbf{u}_n\}$. The ith vector $\mathbf{u}_i$ includes two parts $_E^B\mathbf{P}_i$ and $_E^B\mathbf{R}_i$, both of which are expressions of $\{\mathbf{E}\}$ relative to $\{\mathbf{B}\}$.

$$J\left(\mathbf{u}_i, \mathbf{u}_j\right) = \frac{\mathbf{u}_i \cdot \mathbf{u}_j}{\|\mathbf{u}_i\|^2 + \|\mathbf{u}_j\|^2 - \mathbf{u}_i \cdot \mathbf{u}_j} \quad (3)$$

where J is the generalized Jaccard coefficient used to measure the similarity between two vectors. Any two pose vectors in $\mathbf{U}$ should have a small J to guard against data invalidity.

$$\Delta \mathbf{P}_i^k = {}^{\mathbf{G}\mathbf{B}}\mathbf{P}^k - {}_E^B\mathbf{P}_i \quad (4)$$

$$_G^B\mathbf{P}^{k+1} = {}_G^B\mathbf{P}^k + \frac{1}{n^2} \sum_{i=1}^n \left\| \Delta \mathbf{P}_i^k \right\| \cdot \sum_{i=1}^n \frac{\Delta \mathbf{P}_i^k}{\left\| \Delta \mathbf{P}_i^k \right\|} \quad (5)$$

where k is the iteration number. The initial fixed point $_G^B\mathbf{P}^0$ can be calculated as the mean of the position vectors in $\mathbf{U}$.

After the termination condition is satisfied or a pre-specified number of iterations is reached we can get an estimate of the spatial position of the fixed point $\{\mathbf{B}\}$.
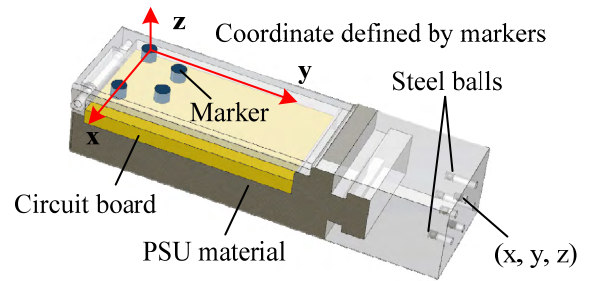
The iteration number specified herein is large enough to avoid stoppage before satisfying the termination condition; if this were not the case, results generated could be inaccurate and unusable. The position offset $_G^E\mathbf{P}$ is calculated according to formula (6).

$$_G^E\mathbf{P} = \frac{1}{n} \sum_{i=1}^n {}_E^B\mathbf{R}_i^{-1} \cdot \left({}_G^B\hat{\mathbf{P}} - {}_E^B\mathbf{P}_i \right) \quad (6)$$

For calculating the transform matrix $_I^R\mathbf{T}$, it is reasonable to combine the navigation system with both the robot and 3D image to complete registration indirectly. Here, we use the NDI system. As already noted, NDI is a binocular stereo vision system that can read the pose information of a marker in $\{\mathbf{N}\}$. Moreover, it can read more than 10 markers simultaneously. To ensure accurate tracking data, a basic marker M_B is set and fixed near the registered object, while other markers are tracked relative to M_B. For this process, we can move the NDI device freely without affecting the coordinates that are read from the system. If more accurate tracking is required, active infrared markers can be used.

As shown in Fig. 6, a registration block is constructed to form the feature points in image space where coordinates can be obtained using a mouse. To quickly identify the corresponding coordinates of these points in space $\{\mathbf{N}\}$, a marker M_R is fixed on this block, and all of the steel balls' coordinates relative to M_R are calibrated before tracking. The registration block is fixed onto the registered object when using the C-Arm scan, and the steel balls' coordinates in space $\{\mathbf{N}\}$ are collected at the same time by tracking M_R.

$$_I^N\hat{\mathbf{T}} = \arg \min \xi \left({}_I^N\mathbf{T}, \mathbf{S_I}, \mathbf{S_N} \right) \quad (7)$$

where $_I^N\mathbf{T}$ is the rigid transform matrix from space $\{\mathbf{I}\}$ to space $\{\mathbf{N}\}$. $\mathbf{S_I}$ and $\mathbf{S_N}$ are two points sets in $\{\mathbf{I}\}$ and $\{\mathbf{N}\}$, respectively. Each element in $\mathbf{S_I}$ has a corresponding item in $\mathbf{S_N}$. ξ is the objective function constituted by the Euclidean norm.

The registration between $\{\mathbf{I}\}$ and $\{\mathbf{N}\}$ involves finding a transform matrix $_I^N\mathbf{T}$ to satisfy the condition that points in $\mathbf{S_I}$ have a minimal distance measurement with $\mathbf{S_N}$ after transformation. The ICP method is used to optimize this

TABLE 2. Parameters for ICP method matrix optimization.

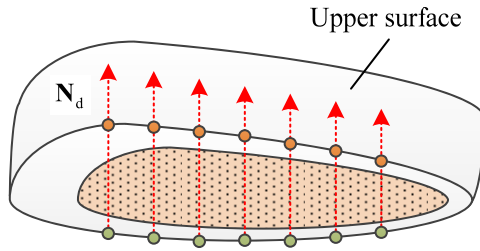| Point Number	Maximum Iterations	Maximum Distance
6	300	1e-5 (mm)

FIGURE 7. Schematic diagram of the lamina with tags. Vector $\mathbf{N_d}$ is pointing from the lower to upper surface. The white and pink areas are cortical and cancellous bone, respectively.

matrix, and the parameters for matrix optimization are listed in TABLE 2.

The registration process between {N} and {R} is similar to the foregoing process. A probe with marker M_P is used to collect the position of the edge of the grinding bit in space {N}, and the corresponding position in space {R} is read from the robot system after offsets are added at the same time.

$$\substack{R\\N}\hat{\mathbf{T}} = \arg\min \xi \left(\substack{R\\N}\mathbf{T}, \mathbf{S_N}, \mathbf{S_R}\right) \tag{8}$$

where $\substack{R\\N}\mathbf{T}$ is the rigid transform matrix from space {N} to space {R}. $\mathbf{S_R}$ is the points set in space {R}. Parameters for ICP optimization are as per TABLE 2.

$$\substack{R\\I}\mathbf{T} = \substack{N\\I}\hat{\mathbf{T}} \cdot \substack{R\\N}\hat{\mathbf{T}} \tag{9}$$

The transform matrix $\substack{R\\I}\mathbf{T}$ can be calculated using formula (9). After this process, the NDI system can be removed. The surgeon can sample the surfaces of the lamina in the 3D image and send these data to the robot system after $\substack{R\\I}\mathbf{T}$ transformation.

B. Intermediate Interpolation

The thickness for grinding is usually about 2-6 mm, and the thick bone structure cannot be removed by a single grinding intervention. An intermediate interpolation process is needed to generate more points between the upper and lower surfaces after transformation. The maximum thickness of one layer is specified as d mm, and the number of layers is calculated according to the maximum Euclidean distance of the point pairs.

As shown in Fig. 7, the bone surface has a certain curvature in {R}. The lower points set is and virtual constraint surface are used as points for path generation, which prevents the grinding bit from causing damage to the spinal nerves. Vector $\mathbf{N_d}$ is parallel to the lines formed by each point pair, and it points from the lower to upper surface. The layers of intermediate interpolation change in shape along $\mathbf{N_d}$ according to

the shape of the upper and lower surfaces. As the distances between point pairs differ, the feed rate varies from place to place. The maximum distance D of pairs is calculated by comparing the lengths of the n_p vectors, where n_p is the pair number without point pairs of two identical coordinates. For decompressive laminectomies, the inner cortical bone of the lamina usually has a grinding margin M, which is smaller than D.

$$n_c = \left\lceil \frac{D - M}{d} \right\rceil + 1 \tag{10}$$

where n_c is the number of grinding layers. M is always smaller than D. If n_c equals 1, the lamina can be removed through a single intervention.

Algorithm 2 Intermediate Interpolation

1:    $\mathbf{N_n} \leftarrow$ *normalize* $\mathbf{N_d}$
2:    **for** $i \leftarrow 1$ **to** $\mathbf{n_p}$
3:        $\mathbf{US}[i] \leftarrow$ *upper surface data* [x y z]
4:        $\mathbf{LS}[i] \leftarrow$ *lower surface data* [x y z]
5:        $\mathbf{NLS}[i] \leftarrow \mathbf{LS}[i] + M * \mathbf{N_n}$
6:    **end**
7:    $\Delta \leftarrow || \mathbf{US} - \mathbf{NLS} || / (\mathbf{n_c} - 1)$
8:    **foreach** *layers*
9:        $\mathbf{MS} += \mathbf{US} - \Delta * layers$
10:       **if** *layers* % 2 = 1
11:          **then** *flip data in current layer in* $\mathbf{MS}$
12:    **end**

Intermediate interpolation is processed by Algorithm 2. Vector **NLS** is the new lower surface after adding grinding margin M, and **SM** is the final vector including the grinding path for the robot. By flipping the data in the odd layers, interpolated data can be linked head to tail for every two layers. This process can reduce the overall length of the robot's path. Every three points in the path are assigned a blend radius to ensure that the robot can move smoothly.

C. OFFSET CORRECTION

For many reasons, registration errors are inevitable, and the accuracy of the robot can also cause position deviation. Generally, the {I} to {R} registration error can be controlled within 0.5 mm by using a registration block with active markers. The offset correction is worth taking into consideration.

The actual start position of the instrument is within a small range of the ideal position P_{start}. As shown in Fig. 8, θ_{offset} is the offset angle, and P_{offset} is the distance between the actual start position and P_{start}. As θ_{offset} and P_{start} are both sufficiently small, compensation can be approximated as the distance between the instrument tip and the bone surface along the line in which the point pair is located. This process can be realized automatically by contact detection based on the force signal. Offset correction can improve grinding accuracy, but the impact is only marginal.
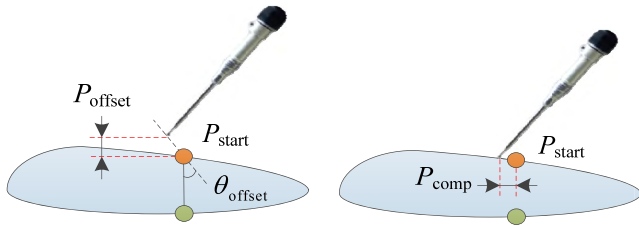
FIGURE 8. Schematic diagram of sufficiently small position offsets. Compensation is approximated as the distance between the instrument and bone along the line in which the point pair is located.

FIGURE 9. The influence of window level and width on the distribution of gray values in an image: 1150/190 (left, used in our system), 890/190 (middle); 1150/760 (right).

IV. GRINDING VELOCITY PLANNING

How long lamina grinding takes depends on not only the length of the planned path, but also the control of velocity. Recently, a number of studies have analyzed on-operation force signals and used these signals for feedback control, such as via the fuzzy logic controller (FLC). This scheme is highly accurate and exhibits good real-time performance, but it increases the complexity of the system because of the integration of force sensing. Additionally, some researchers have hitherto controlled the robot according to changes in the current during the grinding process. Although the current is positively correlated with force, expression of the signal is not stable enough because of electromagnetic interference or characteristics of the motor itself. Medical images contain important information with prior knowledge and, accordingly, image-driven velocity control is proposed.

Anatomically, the lamina has two bone structures: cortical and cancellous. The cortical bone is dense and can resist external shocks well, while the cancellous bone has a loose porous structure that can rapidly attenuate external vibration. Therefore, the cortical bone has a larger gray value than the cancellous bone in X-ray images. After appropriate adjustment of the window level and width, we can obtain a gray expression related to the force signal. X-ray images often contain noise related to the sensitivity of the device imaging module. If the mapping between image and force was only based on the gray value of a pixel, many undesirable virtual force signals would be apparent, causing the robot to make erroneous decisions vis-à-vis velocity control. As virtual forces corresponding to interpolation positions are calculated before robot movement, it is not necessary to use the FLC for online velocity control. When the virtual cutting force is large, the robot needs to slow down to reduce the cutting depth in unit time. Moreover, we have established the mapping between the virtual force and velocity based on dynamics.

A. VIRTUAL FORCE MAPPING

The virtual force is based on gray values distributed on the sagittal, coronal, and transverse planes. Rather than being fixed, the distribution of gray values in the images varies depending on the window level and width settings. The thickness of the bone edge in images is negatively related to level, and the coverage range of the bone is positively related to
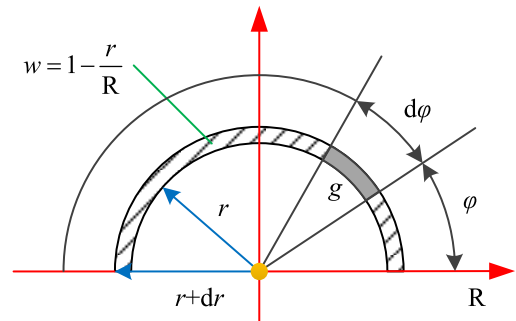
FIGURE 10. Virtual force mapping based on a weighted circular region. R is the radius of the user-specified region. g is the pixel gray value of pixel, which varies with r and φ. w is the weight of the virtual force.

width. The gray values can be treated as prior knowledge of the grinding force. The robot should slow down to maintain system stability; otherwise, it will cause the drive current of the motor to approach or exceed the rated value, indicating that the output power is insufficient to complete cutting of the bone. In this case, if the robot keeps moving, it may cause abnormalities in the system and even damage to the patient.

As shown in Fig. 9, the cancellous bone has a smaller gray value than the cortical bone. Therefore, the force generated when the robot grinds in cancellous bone is smaller than in cortical bone. Due to equipment noise and environmental heterogeneities, the intensities of the X-ray image are uneven. This causes erroneous mapping of the virtual force. To solve this problem, we select the circular region adjacent to the target pixel as the mapping source. Based on this algorithm, the robustness of the mapping can be effectively improved.

As shown in Fig. 10, the circular region is controlled by R, which we have set at 2.5 mm. The center point of the circle is the selected pixel point. The weight of the virtual force decreases for pixels farther away from center, and the weight w belongs to [0, 1]. By a weighted process, we can reduce the effect of cortical bone on the edges of the region. In the robot controller, each interpolated point is mapped back into space {**I**}, and a computing request is sent to the image program via the shared memory to calculate the related virtual force. The program returns the result when the operation is completed.

The gray value in the image with window parameter settings is generally rescaled to [0, 1]. For sensitivity control vis-à-vis the cortical bone, a threshold t is added to the interval.
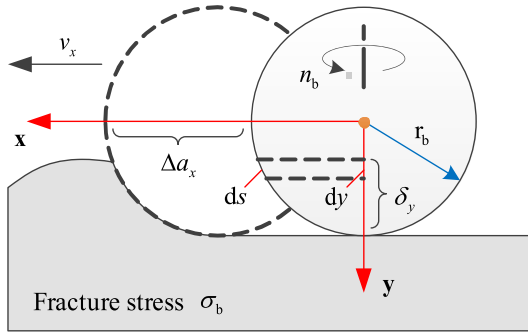
FIGURE 11. Physical model for non-linear velocity control. The radius of the grinding bit is r_b, and movement proceeds along the x axis at velocity v_x. The y-axis depth is δ_y, and the average fracture stress of bone is σ_b.

When the gray value is larger than t, g always equals 1.

$$S_{max} = \int_0^R 2\pi r w(r) \, dr \approx \sum_{s \in \Omega} w(s) \quad (11)$$

where S_{max} is the maximum virtual force with a specified R. s is a pixel in circular region Ω. $r(s)$ is the radius related to s.

$$S(p) = \int_0^R \int_0^{2\pi} r w(r) g(p, r, \varphi) \, d\varphi \, dr \approx \sum_{s \in \Omega} w(s) g(s, p) \quad (12)$$

where S is the current virtual force in current pixel p.

$$F_v(p) = \frac{\hat{S}(p)}{\hat{S}_{max}} \quad (13)$$

where F_v is the normalized virtual force.

In actual computation, g is discrete and cannot be expressed by a function. Normally, we set two accumulators to deal with these pixels, and the normalized result is calculated by (13). The virtual force can be controlled by window level and image width. For lamina grinding, the gray value of cancellous bone with larger voids is often adjusted to 0, while it is set to 1 for the outer surface of bone.

B. DYNAMICS

The external environment of grinding operations is a type of impedance and source of uncertainties. As dynamic interaction between two physical systems must be complementary, the robot system must be an admittance; thus, the input is effort, while the output is flow. Herein, the virtual force is treated as effort, and the velocity is the object to be controlled. We propose a non-linear strategy to control the velocity based on the dynamic characteristics of grinding. The physical model for control is built under ideal conditions.

As shown in Fig. 11, the ball-end grinding tool is used with radius r_b and rotation speed n_b. The thickness of grinding layer δ_y varies with position and is calculated in the path generation process. The shape of the cutting edge and the friction

of chips are both discounted to simplify the mathematical model for expository purposes. The cutting depth in unit time related to the velocity of the robot needs to be controlled in a reasonable range according to motor performance.

$$ds = \frac{r_b}{\sqrt{r_b^2 - y^2}} dy \quad (14)$$

The infinitesimal element ds is expressed by (14). The main and effective cutting area can be calculated by integrating the surface that contacts the cutting edges of the grinding bit along the velocity direction.

$$dM = \pi a_x \sigma_b \left(r_b^2 - y^2 \right) ds \quad (15)$$

where dM is the infinitesimal torque generated by the cutting depth a_x and ds during grinding.

$$\varphi(\delta_y) = 1 - \frac{\delta_y}{r_b} \quad (16)$$

$$\Delta M = \Delta \int_{\delta_y} dM = \frac{\pi \Delta a_x \sigma_b r_b^2}{2} \left(\arccos \varphi - \sqrt{\varphi^2 - \varphi^4} \right) \quad (17)$$

where ΔM is the rate of change in torque, Δa is the rate of change in cutting depth and δ_y is the thickness, which is no less than 0.

For dynamic control, the device output power should be stabilized under rated power P_0. Thus, there exists a control factor $k_c \in (0,1]$ to specify the target torque M_c.

$$M_c = k_c \frac{\eta P_0}{n_b r_b} \cdot F_v(p) + k_m \Delta a_x + \Delta M \quad (18)$$

where η is the energy conversion efficiency of the device, measured experimentally before the product leaves the factory. The friction coefficient k_m is a constant related to the length and material of the grinding tool. The second item on the right side is a simplified expression of the rod deflection equation, which is used to calculate the torque caused by internal friction.

$$\Delta v_x = \frac{\Delta a_x n_b}{60} = \frac{C_b (1 - F_v)}{C_m + \arccos \varphi - \sqrt{\varphi^2 - \varphi^4}} \quad (19)$$

where C_b is a constant derived by formula (18) related to motor performance, grinding bit size, and cutting materials. The maximum Δv_x can be expressed by setting φ and F_v to 1 and 0, respectively; C_b can then be replaced by C_m and the velocity range.

$$v_c = \Delta v_x + v_{min} = \frac{C_m (v_{max} - v_{min})(1 - F_v)}{C_m + \arccos \varphi - \sqrt{\varphi^2 - \varphi^4}} + v_{min} \quad (20)$$

where v_c is the velocity to be controlled based on virtual force. v_{max} and v_{min} are the maximum and minimum user-specified velocities, respectively.

Velocity mapping is shown in Fig. 12. For position-dependent lamina thickness, the depth in each layer is not fixed, indicating that φ varies when grinding; φ is calculated before grinding for velocity control purposes.
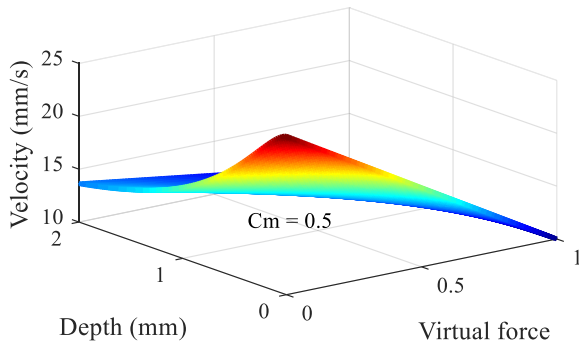
FIGURE 12. Non-linear velocity control based on the dynamic characteristics of grinding. C_m is used to adjust the control law (which equates to the shape of the surface). v_{max} and v_{min} are set to 25 and 10 mm/s, respectively.
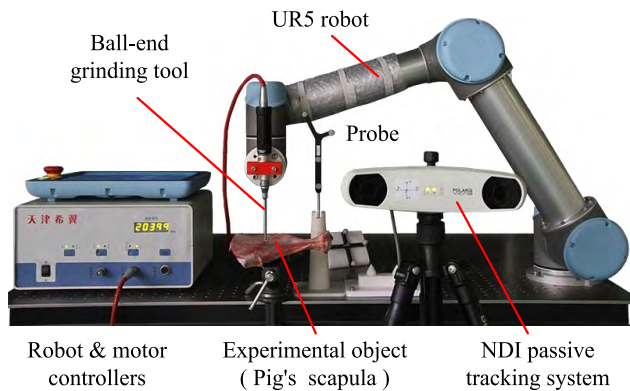

FIGURE 13. Experimental platform for decompressive laminectomy constituted by an SRAS system, an NDI tracking system, and a UR5 system.

V. EXPERIMENT

A. SETUP AND PROCESS

To implement a robot-based decompressive laminectomy, a Universal Robot UR5 (Denmark) with payloads of up to 5 kg is used in our experiment to test the planned path and velocity control. An integrated program named as **Surgical Robotic Auxiliary System** is developed, which includes 3D image interaction using VTK/ITK libraries, probe tracking through serial communication, and a UR5 control system via a 30003 real-time control port. The relevant algorithms delineated above are also integrated. The average experimental object margin is used to assess feasibility, and force signals are used to evaluate the running state with different C_m values.

In Fig. 13, a pig scapula fixed by a bench clamp is used as the experimental object after removing all soft tissues. The registration between 3D image and robot using a probe with a passive marker is accomplished as per the foregoing description. The robot and motor controllers are only used to turn on the robot system and manually adjust the rotation speed of the ball-end grinding tool, respectively. The grinding tool is fixed on the end of the robot with a custom holder produced by a 3D printer. Holder screws provide sufficient
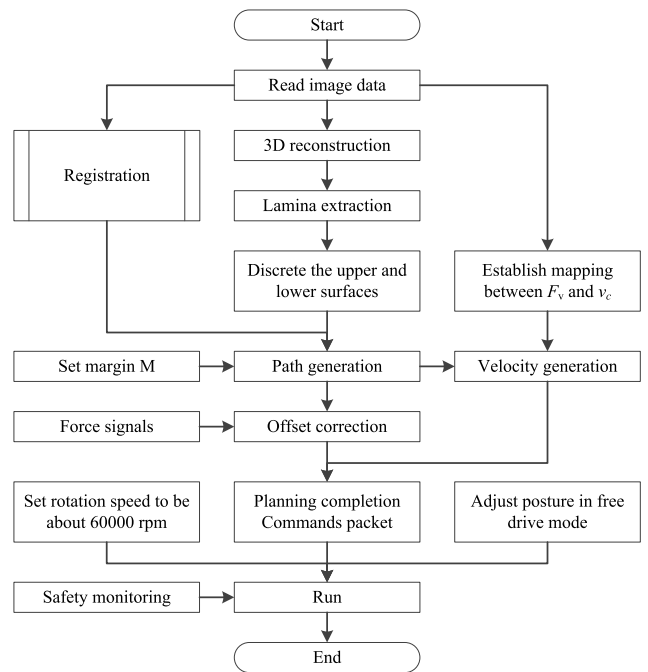

FIGURE 14. Block diagram of operation process. Image data are X-ray image series annular scanned by C-Arm. The free drive mode is only effective before running. The rotation speed is set as required for the surgical instrument.
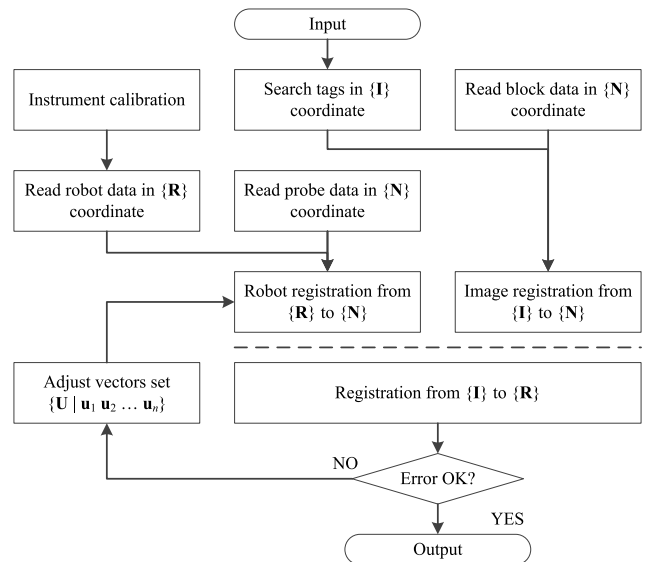

FIGURE 15. Block diagram of the registration sub-process. Image registration error is usually sufficiently small when using the registration block. Data collected in robot registration should be asymmetrical.

clamping force to overcome the axial force exerted on the tool during grinding.

The operation process is delineated in Fig. 14. Fig. 15 provides details of the registration sub-process in Fig. 14. The surgeon interacts with the image after 3D reconstruction by using the bounding box to realize lamina extraction and discrete expression. The registration is divided into two parts:

TABLE 3. Experimental bone grinding parameters.

Data Item	Value
I-N Registration Error (mm)	0.235
N-R Registration Error (mm)	0.573
Rotation Speed (rpm)	60000 ± 3000
Velocity Range (mm/s)	[10, 25]

TABLE 4. System response (1 mm movement) and stability comparison.

Item	Packet time	Comm. response		Sampling period	Standard deviation
		Running	Interrupt		
Constant	~870 ms	Nan			4.566 N
Ours	~980 ms	Nan		~22 ms	2.788 N
FLC	Nan		~46 ms	~30 ms	3.864 N

TABLE 5. Bone grinding results for different Cm.

Cm	Avg F (N)	Max F (N)	Std F (N)	Margin M (mm)
0.1	15.233	22.423	2.203	1.262 ± 0.157
0.3	15.245	22.324	2.174	1.184 ± 0.155
0.5	15.190	22.455	2.653	1.108 ± 0.136
0.7	17.670	24.425	2.788	1.149 ± 0.131
0.9	19.042	25.112	3.133	1.225 ± 0.142

image and robot registration. The image registration error is usually sufficiently small using the registration block, but this conclusion does not transfer to robot registration. A marker can be permanently fixed on the base of the robot and registered into the robot coordinate {**R**} only once with the above method. In subsequent use, the robot can be registered directly by the tracking system. During the running stage, fusion recognition [35, 37] keeps working for safety monitoring in an independent thread with high priority. Where data are abnormal, the program will initiate the stop command and cut off the power supply.

B. FEASIBILITY VERIFICATION

The parameters for bone grinding are listed in TABLE 3. The **I-N** and **N-R** mean points data are transformed from space {**I**} to {**N**} and from space {**N**} to {**R**}, respectively. According to prior commercial and research experiences, an error around 1 mm is acceptable. The rotation speed of the tool changes throughout the grinding process because of the lag in current for feedback control and other factors. The fluctuation is kept at 3000 rpm. The end-of-robot velocity is controlled in a range of 10-25 mm/s.

When the grinding operation begins, the end of the tool is in contact with the upper cortical bone, causing a rapid increase in the force signal mainly along the z-axis. The grinding margin M is set to 1 mm in our experiment, which accords well with expectations of the thickness of the lower cortical bone. The real force signals along the x-axis and y-axis fluctuate in a limited range, and C_m has no significant influence on them. As shown in Fig. 16, three methods are used to test the velocity control, and each curve is independent. These forces mainly fluctuate around 15-30 N. As the burr needs to move a small distance during layer switching, it has an instantaneous impact on the grinding bone, which causes the peaks after contact with the upper bone. In addition, the uneven distribution of tissues has an effect on the force signals. The FLC is tested as [43, 44] with a larger velocity mapping. The time consumptions of the methods are listed in TABLE 4. The packet time is less than 1 s. As the packet process precedes robot movements, it is negligible from a clinical perspective. The communication response is tested as follows. A new thread is created to keep detecting the running status of the robot and Boolean flag in register. The program starts when the ''1 mm movement'' command is sent out, and the register is set to be true. The timer stops when the movement is completed, and the time spent in this process is
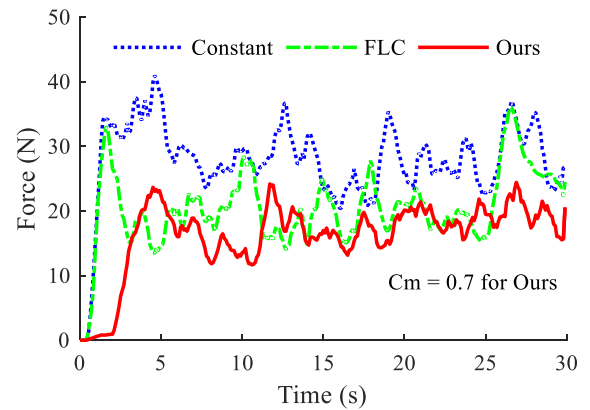

FIGURE 16. Force values during scapula grinding with Cm equal to 0.7. The average force is calculated using original force signals in three orthogonal directions.

calculated as the running response. It has a similar method for calculating the interrupt response. Only FLC needs to keep real-time communication during the grinding operation. The stability of this process is evaluated by the standard deviation of force signals. In empirical testing, our method is superior in most cases. The response delay has a substantive impact on the FLC method because there is an error of approximately 1 mm in each response cycle, which is non-trivial in this context.

The values listed in TABLE 5 are averages obtained by multiple measurements. As shown in Fig. 17, the margin M is calculated as the average of four thicknesses measured at different positions. Theoretically, the greater the C_m, the shorter the time used in grinding the same bones, and the mean and variance of the force are positively related to C_m. However, it is important to note that the margin M is not the same as the force. When C_m is about 0.5, the margin is closest to the set value; when C_m is small, the controlled velocity has a substantive difference in the transition region, which causes system instability in this case. When C_m is large,
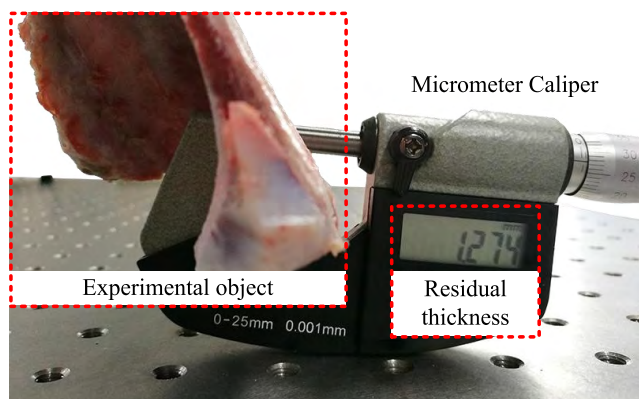
FIGURE 17. Margin M after grinding, calculated as the average of four different grinding surface positions. The precision of the measuring tool is 0.001, and the range is 0-25 mm.

the minimum velocity in the denser region does not adapt well to bone changes, which cause systemic instability. The maximum force shows that this path and velocity planning method can appropriately perform the grinding operation with C_m equal to 0.5, and an acceptable margin of the bone with an error less than 1 mm. The error mainly emanates from the registration procedure; active markers and additional tags should be used to improve the accuracy of registration.

VI. CONCLUSION

This paper proposes an interactive 3-D-image-based method for surgeons to plan the path and velocity of robot systems. Low definition images scanned by C-Arm are used for 3D reconstruction. Surgeons can adjust a bounding box in a 3D image (using a mouse) to select regions of interest, and the lamina is expressed by discrete points that can describe various surfaces. Discrete point distributions are calculated automatically according to the shape of the bounding box. The BSP-Tree is used to search the intersection points to minimize computational demands.

The registration method is designed to convert coordinates from image space into robot space, and a path generation strategy incorporating margin design and offset correction is introduced. For convenient mapping between two spaces, a tracking system is used as the transition frame with a fixed active marker as the basic coordinate. A landmark-based method utilizing an ICP algorithm is used in registrations. As the bone layer is too thick to accomplish the necessary grinding in a single intervention, an interpolation algorithm is used to generate a grinding path between the upper and lower surfaces, taking the specified margin and error correction into account.

As medical images play a critical role in understanding bone information before operations, an image-driven method is proposed to control the velocity of the robot. The cortical bone is dense enough to resist external shocks, while the cancellous bone is loose and can break easily. The composition of the bone can be well reflected by the gray values of the image.

A normalized and robust force expression is introduced to predict grinding states, and this can be adjusted by changing the window level and width. A mapping model is built according to the dynamics of the tool during grinding. The control parameter C_m is designed for adjusting the velocity law.

Experiments are conducted based on the proposed methods. A complete system is developed to explore the feasibility of this method. Results suggest that our method performs better than constant and FLC methods. It maintains relatively stable force signals during grinding, and the margin is closest to the target when C_m equals 0.5.

The registration error is still too large to achieve precise position of the robot, and the efficacy of the landmark-based method should be improved to reduce the time demands placed on the surgeon. To achieve a precise position, the quality of the 3D reconstruction and the calibration of navigation and robot systems should be improved. The experiment does not consider the effect of elastic deformation of the spine. In future work, we will seek to optimize the registration and compensate for spine movement based on elastic mechanics modeling. The application aims to help surgeons develop efficient and personalized options in robot-assisted surgeries.

REFERENCES

[1] C. Whaley, "Decompressive lumbar laminectomy: Indications and discussion," *Techn. Regional Anesthesia Pain Manage.*, vol. 17, no. 2, pp. 39–42, 2013.

[2] S. J. Atlas and A. Delitto, "Spinal stenosis: Surgical versus nonsurgical treatment," *Clin. Orthopaedics Rel. Res.*, vol. 443, pp. 198–207, Feb. 2006.

[3] Z. Y. Fu, J. G. Shi, and L. S. Jia, "Limited laminectomy versus standard laminectomy with posterior instrumentation for lumbar spinal canal stenosis," *Orthopedic J. China*, vol. 22, no. 15, pp. 1347–1352, 2014.

[4] S. Kim, S. M. Hedjri, P. C. Coyte, and Y. R. Rampersaud, "Cost-utility of lumbar decompression with or without fusion for patients with symptomatic degenerative lumbar spondylolisthesis," *Spine J., Official J. North Amer. Spine Soc.*, vol. 12, no. 1, pp. 44–54, 2012.

[5] M. Rahman, L. E. Summers, B. Richter, R. I. Mimran, and R. P. Jacob, "Comparison of techniques for decompressive lumbar laminectomy: The minimally invasive versus the 'classic' open approach," *Minimally Invasive Neurosurg.*, vol. 51, no. 2, pp. 100–105, 2008.

[6] K. Li *et al.*, "Safety and efficacy of cervical laminoplasty using a piezosurgery device compared with a high-speed drill," *Medicine*, vol. 95, no. 37, p. e4913, 2016.

[7] B. D. Elder *et al.*, "Management of cerebrospinal fluid leakage during anterior cervical discectomy and fusion and its effect on spinal fusion," *World Neurosurg.*, vol. 89, pp. 636–640, May 2016.

[8] M. W. Roche, "Robotic and sensor-assisted technologies in knee arthroplasty," *Operat. Techn. Orthopaedics*, vol. 25, no. 2, pp. 127–149, 2015.

[9] Y. Chen *et al.*, "Robotic system for MRI-guided focal laser ablation in the prostate," *IEEE/ASME Trans. Mechatronics*, vol. 22, no. 1, pp. 107–114, Feb. 2016.

[10] A. S. Naidu, R. V. Patel, and M. D. Naish, "Low-cost disposable tactile sensors for palpation in minimally invasive surgery," *IEEE/ASME Trans. Mechatronics*, vol. 22, no. 1, pp. 127–137, Feb. 2017.

[11] J. H. Koenig and M. S. Hepinstall, "Available robotic platforms in partial and total knee arthroplasty," *Operat. Techn. Orthopaedics*, vol. 25, no. 2, pp. 85–94, 2015.

[12] M. Roche, "Robotic-assisted unicompartmental knee arthroplasty: The MAKO experience," *Clin. Sports Med.*, vol. 33, no. 1, pp. 123–132, 2015.

[13] D. P. Devito *et al.*, "Clinical acceptance and accuracy assessment of spinal implants guided with spineassist surgical robot: Retrospective study," *Spine*, vol. 35, no. 24, pp. 2109–2115, 2010.

[14] S. Kim, Y. Ohtake, Y. Nagai, and H. Suzuki, "A novel interpolation scheme for dual marching cubes on octree volume fraction data," *Comput. Graph.*, vol. 66, pp. 169–178, Aug. 2017.

[15] W. E. Lorensen and H. E. Cline, "Marching cubes: A high resolution 3D surface construction algorithm," *ACM SIGGRAPH Comput. Graph.*, vol. 21, no. 4, pp. 163–169, 1987.

[16] T. Lewiner, H. Lopes, and A. W. Vieira, "Efficient implementation of marching cubes' cases with topological guarantees," *J. Graph. Tools*, vol. 8, no. 2, pp. 1–15, 2003.

[17] A. Lopes and K. Brodlie, "Improving the robustness and accuracy of the marching cubes algorithm for isosurfacing," *IEEE Trans. Vis. Comput. Graphics*, vol. 9, no. 1, pp. 16–29, Jan. 2003.

[18] G. L. Vignoles, M. Donias, C. Mulat, C. Germain, and J.-F. Deless, "Simplified marching cubes: An efficient discretization scheme for simulations of deposition/ablation in complex media," *Comput. Mater. Sci.*, vol. 50, no. 3, pp. 893–902, 2011.

[19] R. R. Gharieb, G. Gend, A. Abdelfattah, and H. Selim, "Adaptive local data and membership based KL divergence incorporating C-means algorithm for fuzzy image segmentation," *Appl. Soft Comput.*, vol. 59, pp. 143–152, Oct. 2017.

[20] W. Marian, "An automated modified region growing technique for prostate segmentation in trans-rectal ultrasound images," M. S. thesis, Dept. Elect. Comput. Eng., Univ. Waterloo, Waterloo, ON, Canada, 2008.

[21] J. Stawiaski, E. Decencière, and F. Bidault, "Interactive liver tumor segmentation using graph-cuts and watershed," in *Proc. Workshop, Med. Image Comput. Comput. Assist. Intervent. (MICCAI)*, 2008, pp. 1–12.

[22] C. Li, R. Huang, Z. Ding, J. C. Gatenby, D. N. Metaxas, and J. C. Gore, "A level set method for image segmentation in the presence of intensity inhomogeneities with application to MRI," *IEEE Trans. Image Process.*, vol. 20, no. 7, pp. 2007–2016, Jul. 2011.

[23] S. P. Dakua and J. Abi-Nahed, "Patient oriented graph-based image segmentation," *Biomed. Signal Process. Control*, vol. 8, no. 3, pp. 325–332, 2013.

[24] G. P. Penney, J. Weese, J. A. Little, P. Desmedt, D. L. G. Hill, and D. J. Hawkes, "A comparison of similarity measures for use in 2D-3D medical image registration," *IEEE Trans. Med. Imag.*, vol. 17, no. 4, pp. 586–595, Aug. 1998.

[25] A. Khamene, P. Bloch, W. Wein, M. Svatos, and F. Sauer, "Automatic registration of portal images and volumetric CT for patient positioning in radiation therapy," *Med. Image Anal.*, vol. 10, no. 1, pp. 96–112, 2006.

[26] F. Maes, D. Vandermeulen, and P. Suetens, "Comparative evaluation of multiresolution optimization strategies for multimodality image registration by maximization of mutual information," *Med. Image Anal.*, vol. 3, no. 4, pp. 373–386, 1999.

[27] S. Demirci, M. Baust, O. Kutter, F. Manstad-Hulaas, H.-H. Eckstein, and N. Navab, "Disocclusion-based 2D-3D registration for aortic interventions," *Comput. Biol. Med.*, vol. 43, no. 4, pp. 312–322, 2013.

[28] M. F. Schwerter, F. Lietzmann, and L. R. Schad, "A novel approach for a 2D/3D image registration routine for medical tool navigation in minimally invasive vascular interventions," *Zeitschrift Medizinische Phys.*, vol. 26, no. 3, pp. 259–269, 2016.

[29] M. Y. Hajeer, A. F. Ayoub, D. T. Millett, M. Bock, and J. P. Siebert, "Three-dimensional imaging in orthognathic surgery: The clinical application of a new method," *Int. J. Adult Orthodontics Orthognathic Surg.*, vol. 17, no. 4, pp. 318–330, 2001.

[30] T. Verhoeven, T. Xi, R. Schreurs, S. Bergé, and T. Maal, "Quantification of facial asymmetry: A comparative study of landmark-based and surface-based registrations," *J. Cranio-Maxillo-Facial Surg.*, vol. 44, no. 9, pp. 1131–1136, 2016.

[31] U. Kim, D. H. Lee, Y. B. Kim, D. Y. Seok, J. So, and H. R. Choi, "S-surge: Novel portable surgical robot with multiaxis force-sensing capability for minimally invasive surgery," *IEEE/ASME Trans. Mechatronics*, vol. 22, no. 4, pp. 1717–1727, Aug. 2017.

[32] R. Roy, L. Wang, and N. Simaan, "Modeling and estimation of friction, extension, and coupling effects in multisegment continuum robots," *IEEE/ASME Trans. Mechatronics*, vol. 22, no. 2, pp. 909–920, Apr. 2017.

[33] V. Colla and B. Allotta, "Wavelet-based control of penetration in a mechatronic drill for orthopaedic surgery," in *Proc. IEEE Int. Conf. Robot. Autom.*, vol. 1. May 1998, pp. 711–716.

[34] K. Alam, A. V. Mitrofanov, and V. V. Silberschmidt, "Experimental investigations of forces and torque in con-ventional and ultrasonically-assisted drilling of cortical bone," *Med. Eng. Phys.*, vol. 33, no. 2, pp. 234–239, 2011.

[35] H. Jin, Y. Hu, W. Tian, P. Zhang, J. Zhang, and B. Li, "Safety analysis and control of a robotic spinal surgical system," *Mechatronics*, vol. 24, no. 1, pp. 55–65, 2014.

[36] T. Staroveski, D. Brezak, and T. Udiljak, "Drill wear monitoring in cortical bone drilling," *Med. Eng. Phys.*, vol. 37, no. 6, pp. 560–566, 2015.

[37] Y. Sun, H. Jin, Y. Hu, P. Zhang, and J. Zhang, "State recognition of bone drilling with audio signal in robotic orthopedics surgery system," in *Proc. IEEE Int. Conf. Intell. Robots Syst.*, Sep. 2014, pp. 3503–3508.

[38] Y. Wang *et al.*, "State detection of bone milling with multi-sensor information fusion," in *Proc. IEEE Int. Conf. Robot. Biomimetics*, Dec. 2015, pp. 1643–1648.

[39] F. Accini, I. Díaz, and J. J. Gil, "Using an admittance algorithm for bone drilling procedures," *Comput. Methods Programs Biomed.*, vol. 123, pp. 150–158, Jan. 2016.

[40] Y. Dai, Y. Xue, and J. Zhang,, "Milling state identification based on vibration sense of a robotic surgical system," *IEEE Trans. Ind. Electron.*, vol. 63, no. 10, pp. 6184–6193, Oct. 2016.

[41] V. Gupta, P. M. Pandey, A. R. Mridha, and R. K. Gupta, "Effect of various parameters on the temperature distribution in conventional and diamond coated hollow tool bone drilling: A comparative study," *Procedia Eng.*, vol. 184, pp. 90–98, May 2017.

[42] T. M. Wang, S. Luan, L. Hu, Z. Liu, W. Li, and L. Jiang, "Force-based control of a compact spinal milling robot," *Int. J. Med. Robot. Comput. Assist. Surg.*, vol. 6, no. 2, pp. 178–185, 2010.

[43] Z. Deng *et al.*, "Fuzzy force control and state detection in vertebral lamina milling," *Mechatronics*, vol. 35, pp. 1–10, May 2016.

[44] L. Fan, "Safety control strategy for vertebral lamina milling task," *CAAI Trans. Intell. Technol.*, vol. 1, no. 3, pp. 249–258, 2016.

[45] S. A. Zaheer, S. H. Choi, C. Y. Jung, and J. H. Kim, "A modular implementation scheme for nonsingleton type-2 fuzzy logic systems with input uncertainties," *IEEE/ASME Trans. Mechatronics*, vol. 20, no. 6, pp. 3182–3193, Dec. 2015.

[46] L. Jin, S. Li, X. Luo, Y. Li, and B. Qin, "Neural dynamics for cooperative control of redundant robot manipulators," *IEEE Trans. Ind. Informat.*, to be published, doi: 10.1109/TII.2018.2789438.

[47] L. Jin and S. Li, "Distributed task allocation of multiple robots: A control perspective," *IEEE Trans. Syst., Man, Cybern., Syst.*, vol. 48, no. 5, pp. 693–701, May 2018.

YU SUN received the B.S. and M.S. degrees from the Harbin Institute of Technology, Harbin and Shenzhen, China, in 2012 and 2015, respectively. He is currently pursuing the Ph.D. degree with the Harbin Institute of Technology at Shenzhen. He has been doing research as a guest Ph.D. student in the Shenzhen Institutes of Advanced Technology, Chinese Academy of Sciences, from 2015. His research interests include surgical robot and control, medical image processing, and navigation and deep learning.

ZHONGLIANG JIANG received the B.S. degree from Northeast Electric Power University, Jilin, China, in 2014, and the M.S. degree from the Harbin Institute of Technology, China, in 2017.

He is currently a Research Assistant with the Center for Cognitive Technology, Shenzhen Institute of Advanced Technology, Chinese Academy of Sciences, China. His research interests include surgical robot and control, signal processing, and human-robot interaction.

XIAOZHI QI received the B.S. degree from Yanshan University, in 2009, and the M.S. and Ph.D. degrees from the Harbin Institute of Technology, China, in 2011 and 2017, respectively.

He is currently holds a post-doctoral position with the Center for Cognitive Technology, Shenzhen Institute of Advanced Technology, Chinese Academy of Sciences, China. His current research interests include medical assistant robots and space deployable mechanisms.

YING HU (M'11) received the B.S. degree from Shanghai Jiaotong University, Shanghai, China, in 1991, and the M.S. and Ph.D. degrees in mechanical engineering from the Harbin Institute of Technology, Shenzhen, China, in 1998 and 2007, respectively.

She is currently a Professor with the Center for Cognitive Technology, Shenzhen Institute of Advanced Technology, Chinese Academy of Sciences, China. She is the author or co-author of over 60 scientific papers published in refereed journals and conference proceedings. Her research interests include parallel robots, medical assistant robots, and mobile robots.

BING LI (SM'16) received the Ph.D. degree from The Hong Kong Polytechnic University, Hong Kong, in 2001. He was a Professor of Mechatronics in 2006. He is currently the Head of the School of Mechanical Engineering and Automation, Harbin Institute of Technology, Shenzhen, China. His research interests include parallel manipulators and control, and mechanical vibration and control.

Dr. Li is serving as an Associate Editor of the *International Journal of Mechanisms and Robotic Systems*.

JIANWEI ZHANG (M'91) received the B.S. and M.S. degrees from the Department of Computer Science, Tsinghua University, Beijing, China, in 1986 and 1989, respectively, and the Ph.D. degree from the Department of Computer Science, Institute of Real-Time Computer Systems and Robotics, University of Karlsruhe, Karlsruhe, Germany, in 1994.

He is currently a Professor and the Head of the TAMS Group, University of Hamburg, Hamburg, Germany. He has authored or co-authored over 200 journal and conference papers, technical reports, four book chapters, and two research monographs. His research interests include multimodal perception, robot learning, and mobile service robots.

Dr. Zhang has received several awards, including the IEEE ROMAN and IEEE AIM Best Paper Awards.

● ● ●